Appendix 4-A

Accurate parametric modeling of folded waveguide circuits for millimeter-wave traveling wave tubes

John H. Booske, Mark C. Converse, Carol L. Kory, Christine T. Chevalier, David A. Gallagher, Kenneth E. Kreischer, Vernon O. Heinen and Sudeep Bhattacharjee

INTRODUCTION

Emerging applications in electronic counter measures, radar, communications, and imaging require lightweight, low voltage (≤ 12 kV), compact and broadband ($\Delta f/f$ >10 %) sources of high average power (≥ 100 W) at millimeter wave frequencies (f ~ 30-100 GHz). The folded waveguide traveling wave tube (FWTWT) [1] is an excellent candidate for these applications. This device uses an electric field plane (E plane) bend serpentine rectangular waveguide as a slow wave circuit, as illustrated in Fig. 1. A linear electron beam passing through small holes in the broad wall of a rectangular waveguide interacts with the co-linear electric field of a propagating, fundamental TE_{10} mode. The polarity of the electric field reverses at each E-plane bend with respect to the electron beam's velocity vector [2]. Hence, the folded waveguide circuit belongs to the same "fundamentally backward" class of circuits as the coupled cavity TWT (CCTWT).

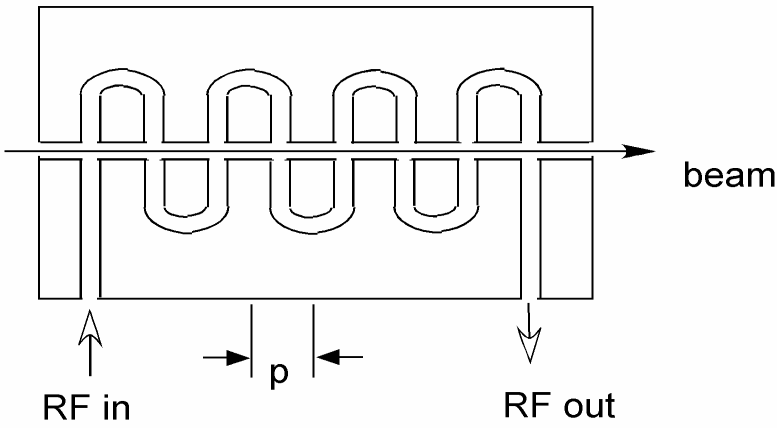

Figure 1. Illustrative sketch of a folded waveguide TWT slow-wave circuit.

Design and analysis of TWTs has been greatly facilitated in the last few years by the emergence of new computational software tools [3]. These include generic electromagnetic problem solvers and TWT-specific models [4-7, 14]. To date, most of the analyses and experimental validation studies have focused on helix-TWTs, and to a lesser extent, CCTWTs.

As a general rule, helix-TWTs are capable of the largest bandwidths, but FWTWTs and CCTWTs provide higher average power handling capability. Compared to conventional CCTWTs, FWTWTs can provide larger bandwidth (20-30% versus 10-15%). In principle, FWTWT circuits are also easier to fabricate than conventional CCTWT circuits. This latter feature has motivated an investigation of the FWTWT as a compact coherent source for the submillimeter or terahertz regime [8,9].

Because of near-symmetry in the azimuthal dimension, helix TWTs can be simulated with 1-, 2-, and 3-dimensional models. In contrast, FWTWTs have no azimuthal symmetries and must therefore be either modeled in one or three dimensions. Three-dimensional (3D) models have the attraction of being highly physical, and can account for complex configuration effects. However, they can be very time and memory intensive, and are therefore of limited utility in early stages of new device design. 1D parametric codes [6], on the other hand, have been developed to a sufficient level of sophistication as to very accurately predict numerous features of helix TWT performance. A review and comparison of helix TWT and FWTWT basic physics [2] leads one to expect equally accurate 1D simulations of FWTWTs, provided appropriate and accurate characterizations are obtained for the frequency-dependent effective phase velocity and interaction impedance parameter functions. With reference to Fig. 1,

$$v_{ph,m} = \frac{\omega}{\Delta\phi_{z,m}/p} \tag{1}$$

is the effective axial phase velocity of the m^{th} spatial harmonic. ω is the angular frequency of the wave (rad/s) $\Delta\phi_{z,m}$ is the phase difference of the m^{th} spatial harmonic's axial electric field $E_{z,m}$ between subsequent beam crossings of the waveguide and p is the distance between subsequent beam crossings, or the "pitch" of the circuit.

$$K_{axis,m} = \frac{\left|E_{z,m}\right|^2}{2\beta_{z,m}^2 P_{wg}} \tag{2}$$

is the effective, on-axis interaction impedance of the m^{th} spatial harmonic. P_{wg} represents the power flowing in the TE_{10} mode associated with a particular on-axis, longitudinal electric field strength, $E_{z,m}$, and $\beta_{z,m}$ is the effective axial wavenumber for the m^{th} spatial harmonic,

$$\beta_{z,m} = \Delta\phi_{z,m} / p \,. \tag{3}$$

Proper analysis requires determination of these parameters for the space harmonic that is synchronous with the electron beam, which in this case is $m = 0$, as discussed in [2].

The types of applications envisaged for FWTWTs (compact, higher average power) lead to large space charge beams. Consequently, accurate design and analyses with 1D parametric TWT models are very sensitive to accurate specification (< 0.5 % error) of the frequency-dependent effective phase velocity function, $v_{ph,m}(\omega)$. Accurate knowledge of $K_{axis,m}(\omega)$ is also important, but not as critical as $v_{ph,m}(\omega)$. This issue will be discussed in later sections.

In the remainder of this paper, the predictions of $v_{ph,m}(\omega)$ and $K_{axis,m}(\omega)$ are described and compared, using approximate analytic expressions, equivalent circuit, 3D finite difference, and 3D finite element models. The phase velocity predictions are compared with experimental measurements of a representative folded waveguide circuit. The various model results are also incorporated into the CHRISTINE1D code to obtain predictions of small and large signal gain in a 40-55 GHz, 100 W FWTWT [10]. It is shown that comparing the gain predictions with experimental measurements of frequency-dependent gain provides a sensitive, confirming assessment of the predicted parameters' accuracy. More importantly, these simulations establish that small signal gain predictions are more sensitive than saturated gain predictions to the accuracy of either parametric function. Moreover, the small signal gain predictions are significantly more sensitive to the accuracy of the phase velocity than the interaction impedance.

Description of the Models and Experimental Methods

Analytic Models

For a smooth wall folded waveguide circuit, the apparent axial electric field's phase shift between beam-crossings for the m^{th} spatial harmonic can be estimated to be

$$\Delta\phi_{z,m} = \left[\left(\frac{\omega}{v_{z,\text{wave}}}\right)p + \pi\right] + 2\pi m \tag{4}$$

Here, $v_{z,\text{wave}}$ is the axial phase velocity of the wave [2],

$$v_{z,\text{wave}} = \frac{p}{L}\frac{c}{\sqrt{1-\left(\frac{\omega_{\text{co}}}{\omega}\right)^2}} \tag{5}$$

where c is the speed of light, ω_{co} is the cutoff frequency for the (TE_{10}) propagating mode,

$$\omega_{\text{co}} = \frac{\pi c}{a}, \tag{6}$$

L is the path length for the wave between beam-crossings, as shown in Fig. 2, and a is the larger transverse dimension of the rectangular waveguide.

Figure 2. Folded waveguide circuit sketch comparing L and p, the wave and beam pathlengths, respectively, between beam-crossings. Also indicated are the transverse dimensions, a and b of the rectangular guide, and the beam hole radius, r_c.

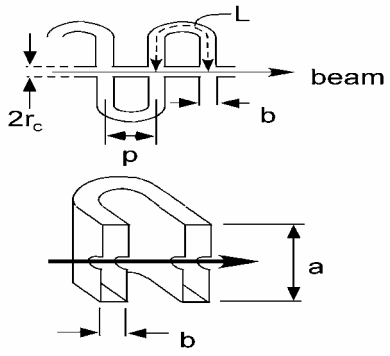

Substitution of Eqs. (4)-(6) into (1) provides an analytic estimate for the FW circuit's effective axial phase velocity seen by the electrons in the beam. This model does not account for the effects of the circuit bends and beam tunnel holes.

$$v_{ph,m} = \frac{p}{L}\frac{c}{\sqrt{1+\left(\frac{\omega_{co}}{\omega}\right)^2} + \frac{\pi c}{\omega L} + \frac{2\pi m c}{\omega L}} \quad . \tag{7}$$

Note that, $v_{z,wave}$ (Eq. 5) is the *projected* axial wave velocity of the wave, whereas $v_{ph,m}$ (Eq. 7) is the effective axial phase-advance velocity seen by the electrons. The electrons see an additional 180 degree phase shift in the wave, based upon the physical structure of the folded waveguide and the beam hole. These two parameters are similar.

In fact, the only difference results from the incorporation of this 180 degree phase shift phenomenon.

An analytic estimate for the on-axis interaction impedance can also be obtained, following the derivation in [2] but accounting for waveguide cutoff effects. The result is

$$K_{axis,m} = K_{wg,10} \frac{1}{(\beta_{z,m} p)^2} \left[\frac{\sin(\beta_{z,m} b/2)}{\beta_{z,m} b/2} \right]^2 \frac{1}{I_0^2(\kappa_{cm} r_c)}, \tag{8}$$

$$K_{wg,10} = \frac{2b}{a} \frac{\eta_0}{\sqrt{1 - \frac{\omega_{co}^2}{\omega^2}}}, \tag{9}$$

$$\kappa_{cm}^2 = \beta_{z,m}^2 - \left(\frac{\omega}{c} \right)^2, \tag{10}$$

where r_b is the beam radius, $\eta_0 \approx 377$ ohms is the "impedance of free space" and K_{wg10} is the waveguide impedance of the TE_{10} mode. I_0 is a modified Bessel function.

Equivalent Circuit Model

Another method of determining the phase velocity of a folded waveguide is with an equivalent circuit model. The different components of the folded waveguide are represented as circuit components, each with their own transmission line transfer matrix. The composite folded waveguide is modeled by serial multiplication of the individual transfer matrices into a single, cascaded or composite transmission matrix. Figure 3 shows a sketch of a section of a folded waveguide. A, B, C, and D designate the critical components: E-plane circular bend, circular bend - straight waveguide junction, straight waveguide section, and electron beam hole, respectively.

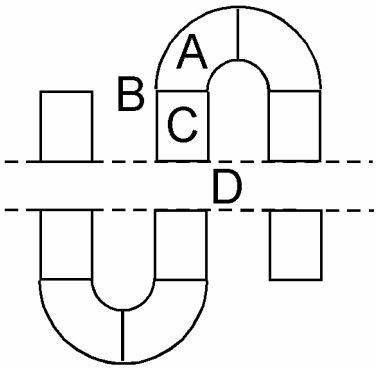

Figure 3. Sketch of a section of the folded waveguide circuit indicating the basic components: (A) E-plane circular bend (B) circular bend – straight waveguide junction (C) straight waveguide section, and (D) electron beam hole

From the "electron beam's perspective", there is just a net phase advance between subsequent crossings of the waveguide. To mathematically describe the effective dispersion properties of this circuit from the electron beam perspective, one would equate the multi-component cascaded transmission matrix to a single transmission matrix constructed by treating the entire folded waveguide as a single transmission line segment [11]. Since the former (cascaded) matrix is solvable, the characteristics of the latter single equivalent matrix can be determined.

For the single equivalent matrix, we can represent the fields in the folded waveguide as a transmission line [11], where

$$V(z) = V(z_o)\cos(\kappa(z - z_o)) + jZI(z_o)\sin(\kappa(z - z_o)), \tag{11}$$

$$I(z) = I(z_o)\cos(\kappa(z - z_o)) + jYI(z_o)\sin(\kappa(z - z_o)). \tag{12}$$

This can be written as

$$\begin{bmatrix} V_1 \\ I_1 \end{bmatrix} = [F]\begin{bmatrix} V_2 \\ I_2 \end{bmatrix} \tag{13}$$

where

$$F = \begin{bmatrix} \cos\kappa & jZ\sin(\kappa) \\ jY\sin(\kappa) & \cos(\kappa) \end{bmatrix} \quad . \tag{14}$$

Here, V_2 is the voltage (which represents an electric field) at the input of a section of the waveguide (usually half of a physical period), V_1 is the voltage at the output, κ is the phase shift, and Y and Z are the admittance and impedance of the folded waveguide equivalent circuit.

Meanwhile, the individual components of the cascaded matrix model of the waveguide (i.e. the straight section, the bend, the hole, etc) can be treated as individual transmission line segments [12]. Specifically the straight waveguide section (C) can be modeled as a uniform section of transmission line of length l_0 and characteristic impedance $Z_0 = K_{wg,10}$, where $K_{wg,10}$ is the TE_{10} waveguide transverse mode impedance of Eq. (9).

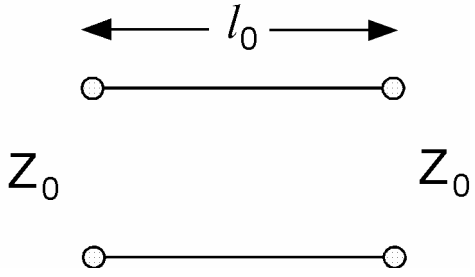

Figure 4. Equivalent transmission line circuit representation of the straight waveguide section (C).

The straight-waveguide-to-E-plane-bend junction (B) can be represented by the equivalent transmission line circuit of Fig. 5.

Figure 5. Equivalent transmission line representation of the junction (B) between the straight waveguide segment and the E-plane bend

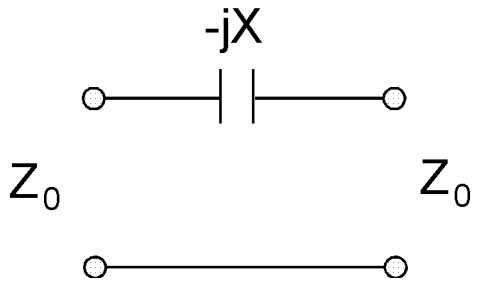

Expressions for the parameters in Fig. 5 are given as [11]:

$$\frac{Z_o'}{Z_o} = 1 + \frac{1}{12}\left(\frac{b}{R^2}\right)\left[\frac{1}{2} - \frac{1}{5}\left(\frac{2\pi b}{\lambda_g}\right)^2\right] \tag{15a}$$

$$\frac{X}{Z_o} = \frac{32}{\pi^7}\left(\frac{2\pi b}{\lambda_g}\right)^3\left(\frac{b}{R}\right)^2 \sum_{n=1,3,\ldots}^{\infty} \frac{1}{n}\sqrt{1-\left(\frac{2b}{n\lambda_g}\right)^2} \tag{15b}$$

a and b are the waveguide cross-sectional dimensions, R is the bend radius and λ_g is the wavelength of the wave in the waveguide.

An equivalent transmission line circuit for the E-plane bend (A) is given in Fig. 6.

Figure 6. Equivalent transmission line circuit representation of an E-plane bend (A).

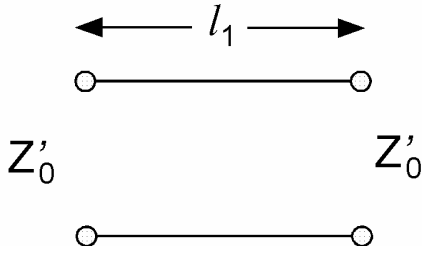

Here $l_1 = 1/2\pi R$ is the length of the E-plane bend.

Finally, a simple circuit model of the (cutoff) beam hole (D) was not available from [11]. Therefore, the circuit equivalent was obtained from a modification of the components of a similar structure provided in [11]. The reference structure is a circular waveguide joined orthogonally to the broad wall of a rectangular waveguide through a small aperture. The difference between the reference structure and the structure to be modeled is that the circular tunnel of the structure to be modeled is a stub whose diameter

equals the aperture diameter and is below the cutoff for propagation and there are two of these stubs present. These differences lead to a modification of the circuit equations of the reference structure. The circuit model of the reference structure [11] is shown in Fig. 7.

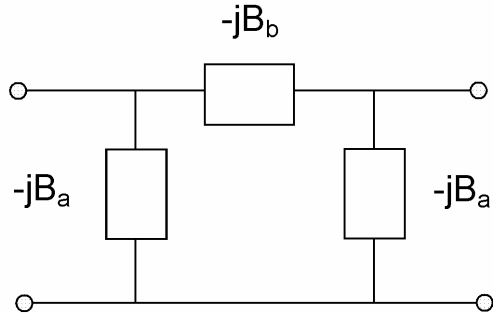

Figure 7: Circuit model of 3-way junction of rectangular and circular waveguide.

The equations for the components B_a and B_b are [11],

$$\frac{B_b}{Y_o} = \frac{\lambda_g ab}{4\pi}\left[\frac{1}{M} - \left(\frac{\pi}{a^2 b} + \frac{7.74}{2\pi R^3}\right)\right] \quad , \tag{16a}$$

$$\frac{B_a}{Y_o} = \frac{\dfrac{2\pi P}{\lambda_g ab}\left(\dfrac{\lambda_g}{\lambda}\right)^2}{1 - \dfrac{4\pi P}{\lambda^2 b}} \quad , \tag{16b}$$

where Y_0 is the admittance of the rectangular waveguide, λ_g is the waveguide wavelength, a and b are the waveguide dimensions, R is the circular waveguide radius (in this case $R=d$ as the aperture is the same size as the circular waveguide/beam tunnel), and λ is the freespace wavelength. M and P are

$$M = \frac{d^3}{6} \quad , \tag{16c}$$

$$P = \frac{d^3}{12} \quad , \tag{16d}$$

where d is the aperture diameter.

To modify the above equations for the structure to be modeled, we observed that the aperture is the same size as the circular tunnel (which is cutoff). Hence, the fringing fields that normally exist on both sides of the aperture, and contribute to the shunt admittance B_b, only exist on one side. Therefore, we chose to halve the value of the circuit component B_b. However, because there are two holes and not one, all component

values were doubled. This leaves us with the original value of B_b and twice the original value of B_a.

As discussed above, the cascaded product of these individual circuit components can be equated to the single equivalent transmission line matrix, [*F*],

$$\begin{bmatrix} \cos\kappa & jZ\sin(\kappa) \\ jY\sin(\kappa) & \cos(\kappa) \end{bmatrix} = [A][B][C][D][C][B][A]. \tag{17}$$

Since the right hand side of (17) can be calculated from the circuit equivalent models of each of the components, we can solve for κ, which is the effective phase advance of the wave as "seen" by the electron beam down the axis of that one section of folded waveguide.

Using a half-period of the structure, the effective axial propagation constant is therefore calculated from

$$\beta_z = \frac{\pi + \kappa}{p} \tag{18}$$

where p is the pitch, or length of half of a period of the folded waveguide. The extra π term accounts for the inherent 180 degree phase shift of the electric field with respect to the electrons, due to the folded nature of the waveguide.

The phase velocity as seen by the electrons is then

$$v_p = \frac{\omega}{\beta_z} \quad . \tag{19}$$

MAFIA

MAFIA (Solution of **MA**xwell's equations by the **F**inite-**I**ntegration-**A**lgorithm) is a 3D, electromagnetic, particle-in-cell (PIC) code. The Finite Integration Technique (FIT) algorithm produces a matrix of finite-difference equations for electric and magnetic field vectors in the structure under study. The solution of these equations yields static, frequency-domain or time-domain solutions of Maxwell's equations. The cold-test (beam free) dispersion is calculated using MAFIA by simulating a single geometrical period, or $2p$, of the structure as shown in Fig. 8. As done previously for helical circuits in [13], the MAFIA eigenmode solver is used to apply quasi-periodic boundary conditions at the longitudinal ends permitting the user to choose a fixed phase shift per turn $\beta_0 p$ in the axial direction. This allows the frequency to be obtained at any axial phase shift, and the corresponding phase velocity to be calculated using Eq. (1). The on-axis interaction impedance is then calculated at this phase shift directly from Eq. (2), where $|E_{z,m}|$ is obtained by doing a spatial Fourier analysis on the total on-axis axial electric field, and the time averaged RF power flow P_{wg} is calculated by integrating the Poynting vector over the circuit cross-section.

MAFIA has the option of automatically defining the mesh based on the user's input of a maximum number of mesh cells. The code then discretizes the geometry into rectangular and triangular cells, keeping the mesh spacing as uniform as possible. For the modeled structure consisting of 2p, we found that the phase velocity converged for a maximum mesh of 300,000 cells. The impedance is less sensitive to the mesh spacing converging with a maximum mesh of 50,000.

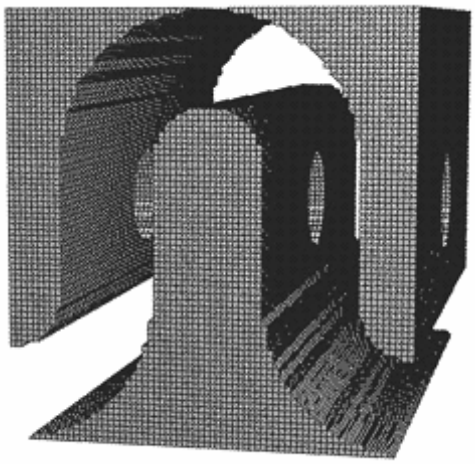

Figure 8. Three-dimensional cutaway view of simulated folded waveguide circuit (maximum mesh=300,000 cells) using MAFIA

HFSS

Ansoft HFSS is a commercial software program that calculates the electromagnetic response of a structure in the frequency domain. Using the Finite Element Method it can calculate S-parameters, near and far fields, eigenmodes of a structure, etc. The mesh used by HFSS is an adaptive mesh consisting of non-regular tetrahedral elements. The program automatically refines the mesh, when and where it is necessary, to achieve a user-specified accuracy. In a method similar to MAFIA, a phase shift across the structure is specified and an associated "eigenfrequency" is determined. Phase velocity and interaction impedance are determined using the same techniques and equations used when simulating with MAFIA.

Microwave Studio

CST MICROWAVE STUDIO™ [14] is a specialized tool for the solution of 3D EM high frequency problems. To suit a variety of applications, the software contains four different simulation techniques: a Transient Solver, a Frequency Domain Solver, an Eigenmode Solver, and a Modal Analysis Solver. It utilizes the new PBA (Perfect Boundary Approximation™) technique to avoid stair step approximations associated with other rectangular meshing techniques. With the PBA, the simulated structure and the electromagnetic fields are mapped to a hexagonal mesh, so it allows a good approximation of even curved surfaces within the cuboid mesh cells [14]. MWS generates an automatic mesh based on the user's specification of frequency range, and mesh per free space wavelength. For a structure of $2p$ in length, we found that the phase

velocity converged for a mesh-per-free-space-wavelength of about 80 at 40 GHz, which translates to a total volumetric mesh of about 120,000 cells. Similar to the MAFIA results, the impedance was fairly insensitive to the mesh spacing. Figure 9(a) shows a contour plot of the surface currents at about 45 GHz. The plot demonstrates that the inside bends have the strongest surface currents, and thus care must be taken that these regions are accurately represented with the mesh. The mesh spacing is also shown in Fig. 9(b).

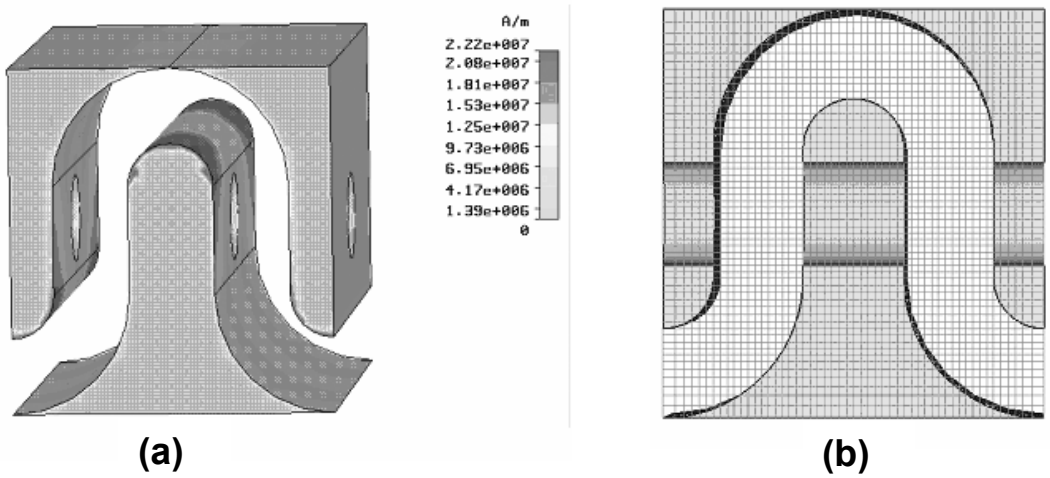

Figure 9. Simulated contour plot of (a) surface currents and (b) side view of mesh using MWS.

Experimental Methods

Phase velocities were measured on an experimental circuit, nominally designed for FWTWT operation in the 40-55 GHz range [1]. The measurements used a conventional technique of drawing a conductive bead on the end of a dielectric rod along the axis of the circuit while launching a wave into one end of the FW circuit. The magnitude of the reflected wave was recorded as a function of position of the bead, producing a standing wave pattern. In the frequency range of interest to this study, this method is known to produce very accurate determinations of the effective axial wavenumber, from which the phase velocity can be directly calculated. In particular, the largest error would be bounded by the measurement of the distance between nodes on the standing wave plot. Based on a position measurement accuracy of less than 0.5 mm, the error in the measured phase velocity values is < 0.2%.

Small signal gain was measured with thermistor detectors and a Hewlett Packard 431 power meter. Input power was supplied with an extended interaction oscillator (EIO).

Results and Discussion

Phase Velocity

Figures 10 and 11, below, compare experimental measurements against the various models. Good agreement between measurements and model predictions was

obtained for the circuit model, HFSS [4], MWS, and MAFIA, with a sufficiently resolved computational grid. For example, a computational mesh of 50,000 points in the MAFIA simulations was found to be inadequate. As discussed previously, it took approximately 300,000 mesh cells in the MAFIA simulations to arrive at phase velocity measurements in good agreement with the experimental data. 300,000 mesh points corresponded to approximately 115 cells-per-free-space-wavelength at 40 GHz. The MWS simulations used 120,000 grid cells, corresponding to approximately 80 cells-per-free-space-wavelength at 40 GHz. For the HFSS computations, a convergence specification of 0.05% on the eigenfrequency was used.

As can be seen, the simplified theory underestimates the effective axial phase velocity, by 1-2 % over the gain bandwidth. Subsequently, it will be shown that the sensitivity to phase velocity of this high space charge device requires a more accurate estimation of velocity and therefore, the simplified theory is not sufficiently accurate.

In contrast, all three of the 3D electromagnetic code predictions replicated the experimental results to better than 0.5% accuracy when sufficient grid resolution or convergence specifications were used (see above discussion).

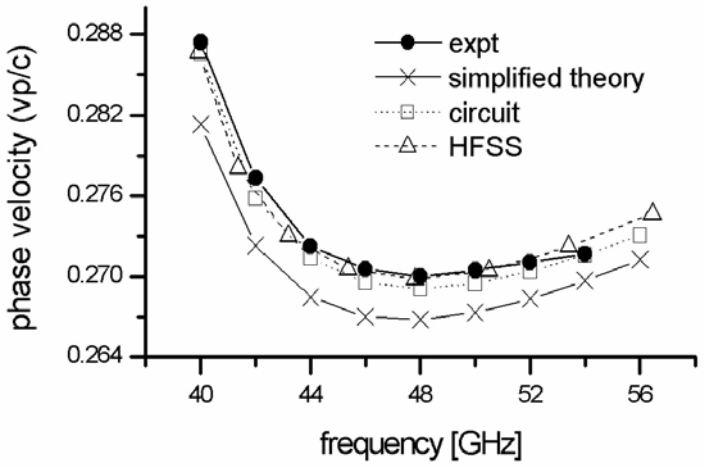

Figure 10. Plot of effective axial phase velocity vs. frequency, comparing experimental measurements, simplified theory, equivalent circuit and HFSS models.

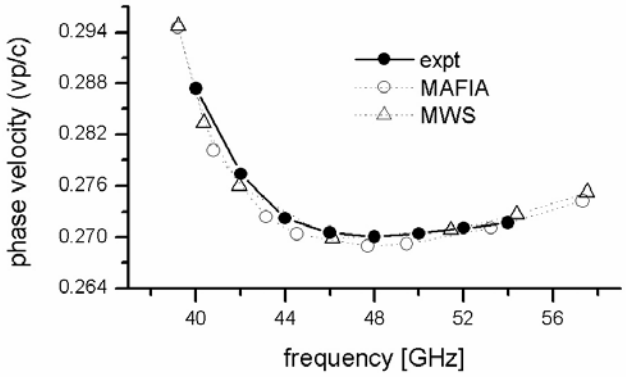

Figure 11: Plot of effective axial phase velocity vs. frequency, comparing experimental measurements and MAFIA and MWS models.

Of the models that accurately calculate the phase velocity, the circuit model seems to be one of the most accurate. Also, since it is analytic, it is easier to work into an optimization algorithm and is faster to compute. This is true, however, only when the device modeled has a small beam hole. The accuracy of the circuit model decreases as the beam hole radius increases and for large beam hole radii the circuit model is not sufficiently accurate. This point is illustrated in Figs. 12 and 13. For small beam radii, the circuit model compares favorably to the HFSS model. For larger beam hole radii, the circuit model estimates a significantly higher phase velocity than the HFSS model.

Based on all examinations to date, the circuit model accuracy is acceptable, i.e., it predicts phase velocity to better than 0.5%, comparable to the 3D numerical code (HFSS in this case) for $r_c/b < \sim 85\%$. Here r_c is the circuit radius and b is the small waveguide dimension.

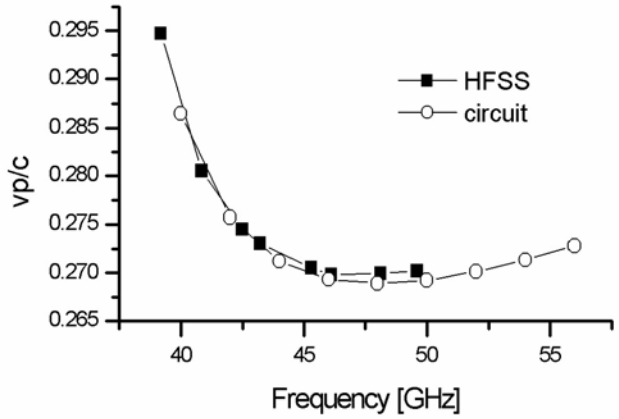

Figure 12: Plot of effective axial phase velocity vs. frequency, comparing equivalent circuit and HFSS results for a FWTWT with a small beam hole radius: $r_c/b = 57.6\%$.

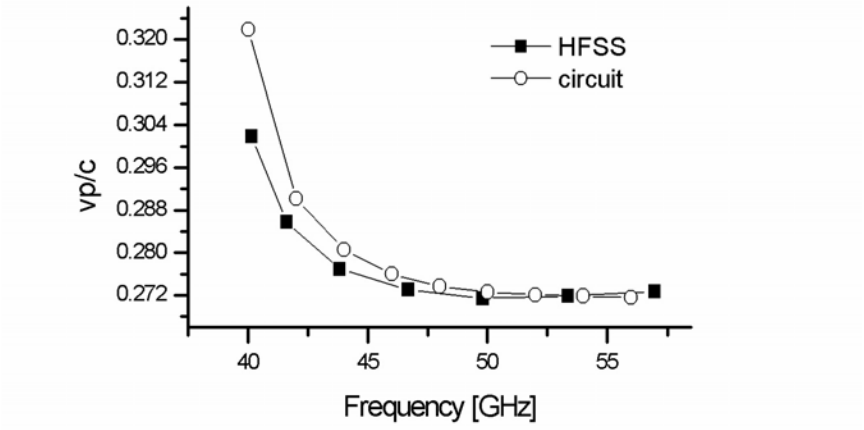

Figure 13: Plot of effective axial phase velocity vs. frequency, comparing equivalent circuit and HFSS results for a FWTWT with a large beam hole radius: $r_c/b = 98.8\%$.

The difference between the circuit and 3D numerical code models in Fig. 13 is most likely due to the choice of the equivalent circuit used to represent the beam hole. (see Section 2.2) That is, this particular model appears to be accurate for small beam holes but suffers from loss of accuracy when $r_c/b \geq \sim 1$. A more accurate solution might be obtained from using the same equivalent circuit model, but modestly and empirically adjusting the values of various coefficients using an adaptive algorithm (e.g., as in [16]) to obtain an improved fit for large as well as small hole diameters. Another alternative would be to examine the application of cutoff beam hole models for klystron cavities [17].

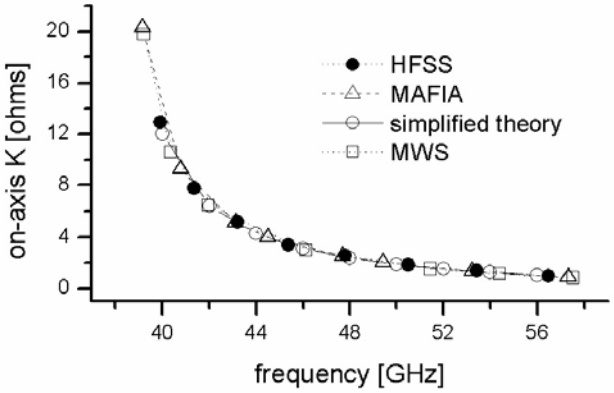

Figure 14: Plot of on-axis interaction impedance vs. frequency, comparing various models.

Interaction Impedance

Figure 14, above, compares the on-axis interaction impedance of various models. As can be seen, there is fairly good agreement between all the models. The greatest variation in estimated impedance seems to be at the lower band edge, and even there the difference is less than 13% between any model and the mean value.

Small and Large Signal Gain

The experimental small signal and saturated gain are compared to the output of CHRISTINE1D [6]. CHRISTINE1D is a one-dimensional physical model, which uses phase velocity and beam averaged interaction impedance to estimate the gain of a TWT. The beam averaged interaction impedance can be obtained by multiplying the on-axis interaction impedance by the factor $I_0\left(\kappa_{cm} r_b\right)^2 - I_1\left(\kappa_{cm} r_b\right)^2{}^2$ where r_b is the beam radius and κ_{cm} is defined in Eq. (10) [18]. I_0 and I_1 are modified Bessel functions. For the simulations the beam voltage, current (unsaturated) and fill factor (r_b/r_c) were 21.2 kV, 200 mA, and 0.5, respectively, consistent with the experimental parameters [1,10]. The experiment included a magnetic confinement factor of 1.5 (above Brillioun), ensuring good beam confinement. Although the experimental device did not include a sever, it did

use a graphite attenuator between the input and output sections [1, 10]. The effects of this attenuator were incorporated into the CHRISTINE1D simulations, based on measurements of the frequency-dependent loss.

Figure 15 compares the experimental small signal gain with the corresponding prediction from CHRISTINE1D. The agreement is remarkably within 4 dB across the entire band from 41 – 54 GHz, except at the very low band edge point at 40 GHz (discussed further below). Figures 16 and 17 show the sensitivity of small signal gain calculations to variations in phase velocity and interaction impedance. As can be seen from the plots, the predictions are extremely sensitive to the specification of phase velocity, but significantly less sensitive to the specification of interaction impedance. In particular, varying the phase velocity by as little as 0.5% results in changes of up to 8 dB in the predicted small signal gain. In contrast, a 10% variation in the interaction impedance results in a more modest 5 dB change in the predicted small signal gain.

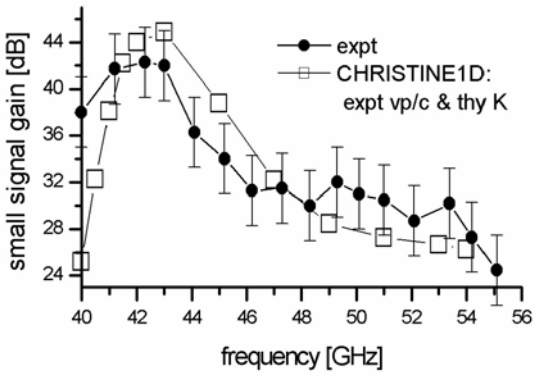

Figure 15: Plot of small signal gain vs. frequency, comparing experimental measurements with CHRISTINE1D TWT model using experimentally determined effective axial phase velocity and the beam averaged interaction impedance from the simplified theory model.

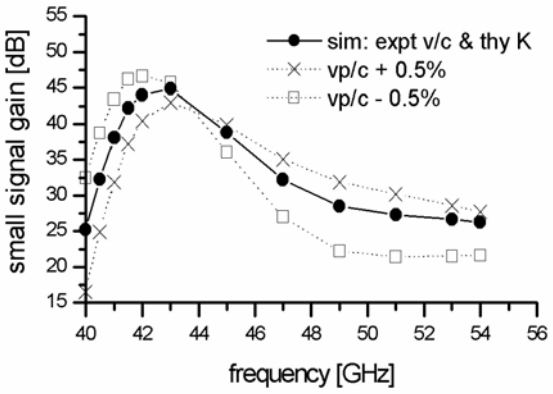

Figure 16: Plot of small signal gain vs. frequency as beam-averaged phase velocity is varied by ± 0.5%.

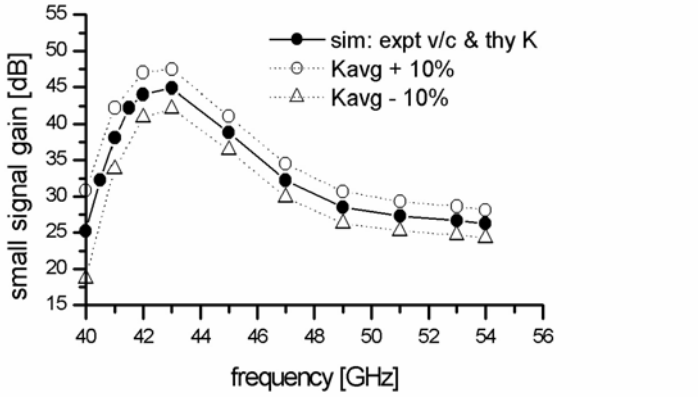

Figure 17: Plot of small signal gain vs. frequency as beam-averaged interaction impedance is varied by ± 10%.

There are several explanations for the discrepancy of a much higher experimental than predicted small signal gain at the low frequency band edge. The experimental gain was determined from measurements of output power using a broadband detector, (the power meter). Hence, it is possible that the experimental values are higher than predicted due to unfiltered second harmonic power. However, this possibility is unlikely, both because the measurements were taken under small signal conditions and because the beam-wave velocity mismatch is considerable and the coupling impedance small near 80 GHz. A more plausible explanation is that 40 GHz is near the waveguide cutoff frequency for the circuit (~38 GHz). This, combined with (or responsible for) coupler mismatch could lead to extra feedback (frequency-dependent input-output coupler mismatch effects were not included in the simulations). Such extra feedback, while insufficient for start oscillation, would be capable of enhancing the measured gain above the theoretical single-pass prediction.

Figure 18 compares CHRISTINE1D predictions of saturated output power to experimental measurements. The agreement is good, being exact near 42 GHz and within 4 dB, even at the low frequency band edge at 40 GHz. Experimental data at higher frequencies were not available due to the lack of a power source at higher frequencies that was able to saturate the TWT.

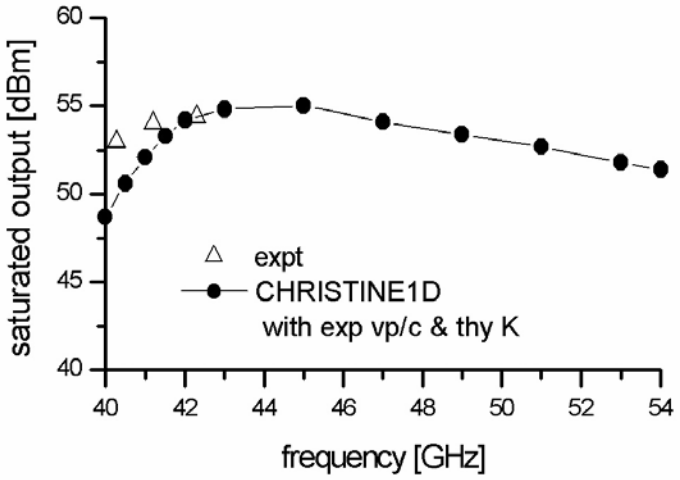

Figure 18: Plot of saturated gain vs. frequency, comparing experimental measurements with CHRISTINE1D TWT model using experimentally determined effective axial phase velocity and the beam averaged interaction impedance from the simplified theory model.

The sensitivity of the saturated performance to phase velocity and interaction impedance was also examined. Table 1 summarizes the results. In general, it was found that the sensitivity of the saturated output power and saturated gain were approximately equivalent when specified in dB. As observed with the small signal gain, the accuracy of the phase velocity has a much more sensitive effect on the predicted saturated power or gain than the accuracy of the interaction impedance. However, the sensitivity of the saturated power or gain is noticeably less than (approximately half) the small signal gain to either parameter. For example, a 10% error in the interaction impedance can result in a 5 dB error in the small signal gain, but only a 1-3 dB error in the predicted saturated power or gain. Similarly, a 0.5% error in the cold circuit phase velocity can result in as much as an 8 dB error in the predicted small signal gain, but only a 2-4 dB error in the predicted saturated power or gain.

Table 1. Effect of input parameter errors on predicted saturated power or gain

	Input parameter error	Saturated power or gain error
Phase velocity error	+ 0.5%	+ 2-3 dB
	- 0.5%	- 3-4 dB
Interaction impedance error	+ 10%	+ 1-2 dB
	- 10%	- 1-3 dB

Given these accuracy constraints on phase velocity and interaction impedance, it is interesting to examine what physical features of the circuits have the greatest influence on both parameters. It is straightforward to derive the following approximate expressions for $v_p(\omega_0)$ and $K(\omega_0)$ (the latter evaluated at the edge of the beam hole) from a simplified model of the circuit. Here, ω_0 is the frequency at which v_p is a minimum, which is

nominally in the "middle" of the operating band of the FWTWT. While these expressions may not provide sufficient quantitative accuracy to meet the 0.5% and 10% guidelines for phase velocity and impedance, respectively, they nevertheless provide useful scaling properties to understand design sensitivity effects. Specifically, for the phase velocity,

$$\frac{v_p(\omega_0)}{c} \approx \frac{p/a}{\sqrt{1+L^2/a^2}} \tag{20}$$

and the interaction impedance,

$$K(\omega_0)\big|_{r=r_c} \approx 47.5\frac{b/L}{\left(1+L^2/a^2\right)^{3/2}}\,. \tag{21}$$

The parameters are defined in Fig. 2. Note, then, that the phase velocity is directly proportional to the pitch, p, as expected, and the interaction impedance is proportional to the small cross-sectional dimension of the waveguide, b. Therefore, any errors in p or b, will lead directly to proportionate errors in v_p or K, respectively. The factor $(1 + L^2/a^2)^{1/2}$ happens to be equal to the frequency ratio ω_0/ω_{co} , where ω_{co} is the cutoff frequency of Eq.(6). For the circuit used for these studies, $\omega_0/\omega_{co} = 1.25$.

Summary and Conclusions

From this study, we have established that accurate, full bandwidth predictions of output power or gain of FWTWT's are possible with one-dimensional parametric TWT models if phase velocity and interaction impedance functions are sufficiently well-characterized. The most sensitive performance parameter was observed to be the small signal gain. It was observed that predictions of the small signal gain to within 4 dB of experimental measurements on a 40-55 GHz FWTWT could be realized over virtually the entire operating band. Similar agreement was observed for saturated gain over a limited frequency band for which experimental data was available.

Sensitivity studies indicate that variations in the phase velocity of 0.5% can result in 8 dB of variation in the predicted small signal gain, while a 10% variation in the interaction impedance can result in a 5 dB change in the predicted small signal gain. The small signal gain prediction is approximately twice as sensitive to variations in these input parameters as the saturated power or saturated gain. Based on these observations, it is indicated that the use of parametric 1D TWT models for accurate, full band predictions of small signal gain in FWTWTs requires knowledge of phase velocity and impedance functions that are accurate to < 0.5% and < 10%, respectively. Saturated gain predictions, being approximately half as sensitive to these parameters, would ostensibly require correct specification of phase velocity and interaction impedance to within ~ 1% and 20% respectively.

An equivalent transmission line circuit model for the FW structure was observed to predict phase velocity very well for smaller beam holes but poorly for large holes, while 3D electromagnetics codes were observed to predict phase velocity functions that

yielded highly accurate TWT gain predictions (e.g., within 4 dB across the band of an experimental test device). To obtain the required accuracy on phase velocity, it was necessary to implement aggressive constraints on convergence or mesh resolution. For example, using the MAFIA simulation code, a mesh spacing of approximately 115 cells-per-free-space-wavelength of linear dimension was required. With MWS, a mesh of approximately 80 cells-per-free-space-wavelength of linear dimension at 40 GHz was suitable. With the HFSS finite element code in eigenmode solver mode, a convergence specification of 0.05% on the eigenfrequency was found acceptable. The simplified analytic model was not acceptable. All methods examined successfully predicted the interaction impedance to within the required 10% tolerance.

REFERENCES FOR APPENDIX 1

[1] G. Döhler, D. Gagne, D. Gallagher, and R. Moats, "Serpentine Waveguide TWT," IEDM Technical Digest, 1987, pp. 485-488.

[2] R.G.E. Hutter, "Beam and Wave Electronics in Microwave Tubes," D. Van Nostrand Company, Inc., New Jersey, 1960.

[3] R.G. Carter, W. Bosch, V. Srivastava, G. Gatti, "Computer Simulation of Intermodulation Distortion in Traveling Wave Tube Amplifiers," IEEE Transactions on Electron Devives, Vol. 48, No. 1 Jan 2001.

[4] HFSS High Frequency Structure Simulator, Ansoft Corporation.

[5] MAFIA, Computer Simulation Technology (CST) GmbH (web:www.cst.de).

[6] T. Antonsen Jr., and B. Levush, "CHRISTINE: A multifrequency parametric simulation code for traveling wave tube amplifiers," NRL/FR/6840-97-9845.

[7] H.P. Freund, E.G. Zaidman, and T.M. Antonsen Jr., "Theory of helix traveling wave tubes with dielectric and vane loading," Physics of Plasmas, Vol. 3, No. 8, August 1996.

[8] J.H. Booske, "New Opportunities in Vacuum Electronics Through the Application of Microfabrication Technologies", International Vacuum Electronics Conference, April 2002.

[9] S. Bhattacharjee, C.L. Kory, W.J. Lee, S. Gallagher, D.W. van der Weide, J.H. Booske, S. Limbach, "Comprehensive simulations of compact THz radiation sources using microfabricated, folded waveguide TWTs", International Vacuum Electronics Conference, April 2002.

[10] G. Döhler, D. Gallagher, and J. Richards, Vac. Elec. Ann. Review Proc. (Crystal City, VA, 1993), pp. V15-V20.

[11] N. Marcuvitz, "Waveguide Handbook", Peter Peregrinus Ltd., London, UK, 1986.

[12] J. J. Choi, C. M. Armstrong, A. K. Ganguly, and F. Calise, "Folded waveguide gyrotron traveling-wave-tube amplifier", Physics of Plasmas, Vol. 2, No. 3, March 1995.

[13] C. L. Kory and J. A. Dayton, Jr., "Computational Investigation of Experimental Interaction Impedance Obtained by Perturbation for Helical Traveling-Wave Tube Structures", *IEEE Trans. on Electron Devices* Vol. 45, No. 9, September 1998.

[14] Microwave Studio, Computer Simulation Technology (CST) GmbH (web:www.cst.de).

[15] J. W. Maruschek, C. L. Kory and J. D Wilson, Generalized Three-Dimensional Simulation of Ferruled Coupled-Cavity Traveling-Wave Tube Dispersion and Impedance Characteristics. *NASA TP-3389*, November 1993.

[16] P.L. Werner, R. Mittra, and D.H. Werner, "Extraction of equivalent circuits for microstrip components and discontinuities using the genetic algorithm," IEEE Microwave and Guided Wave Letters, Vol. 8, no. 10, 333-335 (1998).

[17] see, for example, K Fujisawa, "General Treatment of Klysron Resonant Cavities," IRE Trans. Micr. Thy. Tech., vol. MTT-6, 344-358 (1958).